Heat transfer mechanisms in an impinging synthetic jet for a small jet-to-surface spacing

P. Valiorgue, T. Persoons *, A. McGuinn and D.B. Murray

Mechanical Engineering Department, Parsons Building, Trinity College, Dublin 2, Ireland, tel: +353-1-8968503, fax: +353-1-6795554

Abstract

Impinging synthetic jets have been identified as a promising technique for cooling miniature surfaces like electronic packages. This study investigates the relation between the convective heat transfer characteristics and the impinging synthetic jet flow structure, for a small jet-to-surface spacing $H/D = 2$, dimensionless stroke length $1 < L_0/D < 22$, and Reynolds number $1000 < Re < 4300$. The heat transfer measurements show evidence for a power law relationship between the Reynolds and Nusselt number for a constant stroke length. A critical stroke length $L_0/H = 2.5$ has been identified. Using phase-resolved particle image velocimetry, vortex quantification is applied to elucidate the influence of the impinging vortex on the time-averaged heat transfer distribution.

Key words: synthetic jet, convective heat transfer, vortex quantification, particle image velocimetry, critical stroke length

PACS: 44.15.+a, 47.32.Ef, 47.80.Cb

* Corresponding author.
Email address: tim.persoons@tcd.ie (T. Persoons).

Nomenclature

A	orifice cross-sectional area, m^2
a	speed of sound, m/s
D	jet orifice diameter, m
d_I	PIV interrogation window size, pixel
f, f_0	jet frequency and cavity Helmholtz frequency, Hz
H	jet-to-surface spacing, m
h	convective heat transfer coefficient, $\ddot{q}/(T - T_{ref})$, W/(m^{2}K)
K	orifice pressure drop coefficient
k	thermal conductivity of air, W/(mK)
L	orifice length, m
L_0	jet stroke length, m
m	pixel resolution in PIV image, m/pixel
Nu, Nu_0	local and stagnation Nusselt number, hD/k
p^*	jet cavity pressure amplitude, Pa
Pr	Prandtl number
Re	Reynolds number, $\rho U_0 D/\mu$
r', r'_1	radial distance from vortex centre and equivalent vortex radius, m
$\ddot{q}$	surface convective heat flux, W/m^2
s	distance covered by propagating vortex centre, m
T, T_{ref}	surface and jet cavity temperature, K
t	time, s
U_0	averaged jet velocity during blowing phase, m/s
$U_m(t)$, U_m^*	mean instantaneous jet velocity and amplitude, m/s
u, v	axial and radial velocity, m/s

V	jet cavity volume, m^3
v_r	tangential velocity around vortex centre, m/s
x, r	axial and radial coordinate, m
x_c, r_c	location of vortex centre, m
z	coordinate perpendicular to PIV measurement plane, m

Greek symbols

Δ	absolute measurement uncertainty
Γ, Γ_1	circulation around vortex centre and circulation at equivalent radius r_1', m^2/s
θ, θ_{max}	phase within jet period, and phase at peak ejection, rad
μ	dynamic viscosity, Ns/m^2
ρ	density, kg/m^3
τ	pulse separation time of PIV light sheet, s
ω	vorticity, $\frac{1}{2}(\frac{\partial v}{\partial x} - \frac{\partial u}{\partial y})$, rad/s

1 Introduction

Synthetic or zero-net mass flux jets are being studied in various fields of fluid dynamics, from active flow control to enhanced heat transfer. A synthetic jet is produced by the interaction of a train of vortices that form by successive ejection and suction of fluid across an orifice. The orifice flow is forced by periodic pressure variations, typically generated in a cavity with a movable diaphragm.

To identify flow mechanisms influencing the surface heat transfer with an impinging synthetic jet, the heat transfer results are interpreted as a function

of the main flow parameters. A free synthetic jet flow is described by the dimensionless stroke length L_0/D and the Reynolds number $Re = \rho U_0 D/\mu$. An impinging synthetic jet flow is further characterised by the dimensionless jet-to-surface spacing H/D.

The stroke length $L_0 = \int_0^{1/(2f)} U_m(t)\mathrm{d}t$ represents the distance traveled by a fluid slug during the ejection phase, where f is the jet frequency and $U_m(t)$ is the instantaneous mean jet orifice velocity. The corresponding velocity scale $U_0 = 2fL_0$ is the averaged jet orifice velocity during the ejection phase. For axisymmetric jets, a jet formation threshold value corresponds to $(L_0/D)/\pi > 0.16$ or $L_0/D > 0.5$ [1, 2]. For a two-dimensional synthetic jet, Gillespie et al. [3] show that the stagnation point flow can be turbulent at Reynolds numbers far below the transition value for steady jets. However this cannot be generalized since the transition to turbulence is a complex process. According to Smith and Glezer [4], a free two-dimensional synthetic jet transitions after $t > 0.5/f$. Therefore the turbulent nature at the stagnation point in an impinging jet likely also depends on L_0/H.

Pavlova and Amitay [5] studied the influence of the stroke length for different H/D. With smaller stroke lengths, the formed jets are more susceptible to breakdown and merging of vortices prior to impingement, thereby removing more heat for small jet-to-surface spacings. Conversely, for larger stroke lengths, the vortex rings impinge on the surface separately, thereby removing more heat for large jet-to-surface spacings. The influence of these distinct flow regimes on the heat transfer is confirmed and detailed in the present paper, resulting in a critical stroke length value.

The jet-to-surface spacing H/D influences the flow at the heat transfer surface,

and the level of confinement and recirculation as shown by Campbell et al. [6]. Pavlova and Amitay [5] and Gillespie et al. [3] studied the influence of H/D on the heat transfer to an impinging synthetic jet experimentally for different settings. Both studies indicate that the maximum heat transfer occurs for jet-to-surface spacings in the range $4 < H/D < 11$. Very few heat transfer studies have been undertaken for $H/D < 4$.

Another phenomenon which merits investigation is the understanding of the role of vortices on the surface heat transfer. For steady jets, this has been studied by O'Donovan and Murray [7]. However, such a study may be particularly fruitful for synthetic jets due to the fixed formation frequency, thus facilitating phase-resolved measurements.

This paper sets out to investigate the heat transfer mechanisms in an impinging round synthetic jet flow for a small jet-to-surface spacing $H/D = 2$. The heat transfer performance will be characterised as a function of the stroke length L_0/D and Reynolds number Re, (i) to identify a critical stroke length marking different flow and heat transfer regimes, and (ii) to investigate the scaling of Nu with Re. Phase-resolved velocity measurements using particle image velocimetry (PIV) are applied to identify flow regimes and to quantify the impinging vortex dynamics.

2 Experimental approach

The synthetic jet flow is produced by a cavity enclosed on one side by an acoustic speaker and on the opposite side by an orifice plate, as depicted schematically in Fig. 1. The oscillating speaker diaphragm forces air flow across

the round orifice (diameter $D = 5$ mm, length $L = 10$ mm), thus forming a synthetic jet directed towards a heated foil. The jet-to-surface spacing $H = 10$ mm ($H/D = 2$). The stroke length and Reynolds number vary over the range allowed by the acoustic speaker, respectively $1 < L_0/D < 22$ and $1000 < Re < 4300$.

2.1 Convective heat transfer measurements

The synthetic jet is directed towards a heated foil surface, consisting of a 170 μm thick polyester substrate with 3.5 nm thick vacuum deposited layer of silver. The ohmically heated foil is sufficiently thin to be considered a constant heat flux boundary condition. The foil is optically transparent, thus allowing the PIV laser light sheet to pass through. The bottom of the foil is painted matte black, except for a 2 mm wide strip along the PIV measurement plane. A FLIR ThermoVision$^{\mathrm{TM}}$ A40M thermal imaging camera measures the temperature distribution T on the bottom of the heated foil. Temperature data within the 2 mm strip are omitted. During heat transfer measurements, the jet is offset to $z = 10$ mm from the PIV centreline to measure the complete temperature distribution, including the stagnation point.

The local convective heat flux $\ddot{q}$ is determined from the electrical power, and is corrected for radiation and convection heat loss from the bottom of the foil and radiation heat loss from the top. Lateral conduction within the foil is verified to be negligible compared to the other loss terms. The relative uncertainty in the Nusselt number is considered equal to the uncertainty in the convective

heat transfer coefficient $h = \ddot{q}/(T - T_{ref})$, given by:

$$\frac{\Delta Nu}{Nu} \simeq \frac{\Delta h}{h} = \sqrt{\left(\frac{\Delta \ddot{q}}{\ddot{q}}\right)^2 + \frac{\Delta T^2 + \Delta T_{ref}^2}{(T - T_{ref})^2}} \tag{1}$$

The uncertainty in the heat flux $\Delta\ddot{q}/\ddot{q}$ arises mainly from non-uniformities in the electrical contact resistance between foil and electrodes, and is estimated to be around 10%. The reference temperature T_{ref} is measured in the jet cavity using a K-type thermocouple. Based on the measurement standard deviation and a 95% confidence level, the uncertainty $\Delta T_{ref} = 0.25\,^{\circ}\mathrm{C}$. The uncertainty ΔT results from a combination of uncertainty in the infrared camera measurement and the radiation properties of the heated foil and its surroundings. Overall, $\Delta T = 0.25\,^{\circ}\mathrm{C}$.

A determining factor in the overall uncertainty Δh is the temperature difference $T - T_{ref}$. The minimum difference occurring at the stagnation point (at $r = 0$) is typically greater than $3\,^{\circ}\mathrm{C}$, resulting in an estimated uncertainty $\Delta h/h = 15\%$. However, in certain adverse flow conditions, recirculation of hot air into the jet cavity may cause $T - T_{ref}$ to reduce to around $2\,^{\circ}\mathrm{C}$, thereby increasing the measurement uncertainty of the stagnation Nusselt number $\Delta Nu_0/Nu_0$ to 20%.

This non-negligible measurement uncertainty is intrinsic to the constant heat flux boundary condition approach, yet also partly due to the unconventional choice of heater foil material (i.e. transparent silver-coated polyester film). For this reason, additional local heat transfer measurements have been performed using a thermopile heat flux sensor on an isothermally heated 5 mm thick copper plate. The RdF Micro-Foil$^{\mathrm{TM}}$ heat flux sensor has been calibrated in a steady impinging air jet against an established correlation for the stagnation

Nusselt number [8], as described by O'Donovan and Murray [7] and McGuinn et al. [9]. The thermopile sensor measurement has an uncertainty on the Nusselt number of around 6% and a spatial resolution of about 1 mm.

2.2 Synthetic jet operating point

Persoons and O'Donovan [10] describe an analytical acoustic model using a cavity pressure measurement (G.R.A.S. 40BH microphone, 0.5 mV/Pa) to estimate the synthetic jet velocity, and thus Re and L_0. This semi-empirical model requires an orifice damping coefficient K. The model accurately predicts the jet velocity for the frequency range from zero over the cavity Helmholtz frequency f_0, up to a geometry-dependent frequency limit [10]. Using the pressure magnitude p^*, the velocity magnitude U_m^* is determined from:

$$\frac{\rho a U_m^*}{p^*} = \sqrt{\frac{2V}{AL'}} \times \sqrt{\left(\frac{f}{f_0}\right)^2 + \sqrt{\left(\frac{f}{f_0}\right)^4 + \left(K\frac{V}{AL'}\frac{p^*}{\rho a^2}\right)^2}}^{-1} \tag{2}$$

where $L' = L + 2\beta D$ is the effective orifice length ($\beta = 0.425$ for a sharp-edged circular orifice) and $f_0 = a/(2\pi L')\sqrt{AL'/V} \simeq 200$ Hz. The orifice damping coefficient $K = 1.46 \pm 0.13$ is determined from a steady flow pressure drop measurement. For quasi-sinusoidal pressure and velocity oscillations $U_0 = U_m^*/(\pi/2)$, yielding $Re = \rho U_0 D/\mu$ and $L_0 = U_0/(2f)$. This approach allows to set the synthetic jet operating point without the need for a priori in-situ velocity measurements. The predicted velocity agrees very well to the velocity measured using PIV close to the orifice.

2.3 Velocity measurements

Velocity measurements have been performed using particle image velocimetry (PIV). The PIV system comprises a New Wave Solo-II Nd:YAG twin cavity laser (30 mJ, 15 Hz) and a PCO Sensicam$^{\mathrm{TM}}$ thermo-electrically cooled CCD-camera (1280×1024 px^2, 12 bit) with 28 mm lens. A glycol-water aerosol is used for seeding, with particle diameters between 0.2 and 0.3 μm. Customised optics are used to generate a 0.3 mm thick light sheet. The CCD-camera is mounted perpendicular to the light sheet. The image magnification is 1:4.1 ($m = 54$ μm/px). A narrow band pass filter is used with fluorescent paint on the orifice plate to maximise the signal-to-noise ratio near the walls. Phase-locked to the synthetic jet actuator, images are acquired for 24 phases per period and 16 vector fields are averaged for each phase. The pulse separation time is determined such that the maximum particle image displacement does not exceed a quarter of the initial interrogation window size [11]. The velocity fields have been processed with LaVision DaVis 6.2 software, using multi-pass cross-correlation with an interrogation window size decreasing from 64×64 to 16×16 px^2 at 50% overlap.

To improve the dynamic velocity range, a multi double-frame PIV technique is applied [12, 13]. To this end, images are acquired for two values of the pulse separation time, $\tau = \tau_{min} = \frac{1}{4} m d_I / U_m^*$ and $\tau = 8\tau_{min}$. The value τ_{min} is optimal for the high velocity jet core region, and an arbitrary choice of $8\tau_{min}$ is better suited for the low velocity wall jet region. Persoons et al. [12] show a considerable increase in dynamic velocity range by applying this technique, resulting in more accurate velocity vectors in the low velocity wall jet and entrainment regions.

2.4 Vortex dynamics

From the phase-resolved velocity fields, the vorticity field ω is obtained using a circulation-based algorithm by Vollmers [14]. The vortex centre $\{x_c, r_c\}$ is determined in a two-step algorithm, (i) first by detecting the local peak vorticity, (ii) secondly by performing a five-point two-dimensional parabolic fit to the local vorticity field to determine the interpolated vortex centre location.

In a frame of reference moving with the vortex centre $\{x_c, r_c\}$, Fig. 2 shows the definition of an equivalent vortex radius r'_1 defined by the peak tangential velocity $\max[v_r(r')] = v_{r1}$. The circulation is linked to the tangential velocity as $\Gamma(r') = 2\pi r' v_r(r')$. The measured vortex profiles are similar to viscous Lamb-Oseen vortices, as described by Saffman [15]. The vortex strength is quantified here by the circulation at the equivalent radius $\Gamma_1 = \Gamma(r'_1)$.

3 Experimental results

Firstly, the influence of the stroke length L_0 and Reynolds number Re on the time-averaged flow field is investigated. Two distinct flow regimes thus identified help to explain the observed heat transfer characteristics, and the existence of a critical stroke length. Finally, the dynamics of the impinging vortices are studied using phase-resolved PIV, to further elucidate the underlying heat transfer mechanisms.

3.1 Flow field characteristics

Time-averaged flow field plots are produced to study the effect of the stroke length while keeping the Reynolds number constant, and vice versa.

3.1.1 Effect of the stroke length

Figure 3 shows the time-averaged vorticity distributions for a constant Reynolds number $Re \simeq 1020$ and increasing stroke lengths $2.48 < L_0/D < 8.70$. The contour lines indicate the dimensionless vorticity $\omega D/U_0$, with a contour spacing increasing from 1/32 to 1 in powers of 2.

For high stroke lengths from $L_0/D > 5$ (Fig. 3c,d), an increasingly stronger time-averaged recirculation vortex can be observed close to the heat transfer surface, around $r/D = 2$. This vortex is not observed for lower stroke lengths, which indicates that two different flow regimes occur, depending on the value of the stroke length.

For a free synthetic jet flow, Shuster and Smith [2] show that the distance traveled by the propagating vortex scales with the stroke length. Thus, for an impinging synthetic jet flow, the ratio of stroke length L_0 to jet-to-surface spacing H is expected to determine the flow regime. As such, in the discussion of the heat transfer characteristics, the stroke length is indicated as L_0/H instead of L_0/D.

3.1.2 Effect of the Reynolds number

Figure 4 shows the time-averaged vorticity distributions for a constant stroke length $L_0/D \simeq 5.0$ and increasing Reynolds numbers $1010 < Re < 3000$. Again, the contour lines indicate the dimensionless vorticity $\omega D/U_0$, with the same contour spacing as for Fig. 3.

Plotting the dimensionless vorticity $\omega D/U_0$ facilitates the comparison between the flow fields at different Re. The flow structure seems quasi independent of the Reynolds number for a fixed stroke length. This has already been established by Shuster and Smith [2] for a free synthetic jet flow, even on the phase-averaged level.

The Reynolds number does not appreciably change the flow structure yet it does change the intensity of the flow, since the vorticity and velocity scale with U_0 ($\propto Re$). This is an important finding to explain the power law relationship between the stagnation Nusselt number and Re, as discussed below.

3.2 Stagnation heat transfer characteristics

For a round steady turbulent impinging jet, a correlation for the Nusselt number can be expressed in the simplest form as $Nu \propto Re^n$ where the exponent $n = fn(Pr, r/D, H/D)$ is typically in the range $0.5 < n < 0.8$. Liu and Sullivan [8] obtained a correlation $Nu_0 = 0.585 Re^{0.5} Pr^{0.4}$ for $H/D < 2$. In this section too, the surface heat transfer is characterised by the stagnation Nusselt number Nu_0 at $r = 0$.

Figure 5 shows Nu_0 as a function of the stroke length and Re. The stroke

length is plotted as L_0/H, relative to the jet-to-surface spacing. These results are obtained for a single jet-to-surface spacing $H/D = 2$. The Nusselt number in the vertical axis is scaled as Nu_0/Re^n, where the exponent $n = 0.32 \pm 0.06$ is obtained through least-squares fitting of the data points to a single curve. The circular markers represent measurements on the constant heat flux heated foil ($1 < L_0/D < 22$, $1000 < Re < 4300$). Additionally, the triangular markers represent measurements on an isothermal plate using a thermopile heat flux sensor ($2 < L_0/D < 20$, $Re = 3000$).

As the stroke length varies from a minimum [1] to higher values, the heat transfer performance in terms of Nu_0/Re^n first increases quasi linearly up to $L_0/H \simeq 2.5$, after which a saturation value is reached. In Fig. 5, a vertical dotted line indicates this critical stroke length at $L_0/H \simeq 2.5$ (or $L_0/D \simeq 5$), separating two heat transfer regimes for low and high stroke lengths. At low L_0/H, the stroke length significantly influences the heat transfer at the stagnation point. At high L_0/H, this influence diminishes and the synthetic jet tends more towards a pulsed (on/off) continuous jet. In this case, the heat transfer at the stagnation point depends primarily on the Reynolds number for a fixed geometry. The dashed line in Fig. 5 represents this bilinear correlation:

$$\begin{cases} \frac{Nu_0}{Re^n} = c & (L_0/H \geqslant 2.5) \\ \frac{Nu_0}{Re^n} = a + (c-a)\frac{L_0/H}{2.5} & (L_0/H < 2.5) \end{cases} \tag{3}$$

where the exponent $n = 0.32 \pm 0.06$, the saturation value $c = 1.52 \pm 0.04$ and the intercept $a = 0.19 \pm 0.07$.

The data points for Nu_0/Re^n collapse reasonably well to Eq. (3). Furthermore,

[1] The formation threshold stroke length for a round synthetic jet is $L_0/D > 0.5$ [1].

the circular and triangular markers corresponding to constant heat flux and isothermal boundary conditions show good agreement. The remaining scatter is consistent with the uncertainty in the stagnation heat transfer coefficient $\Delta Nu_0/Nu_0 \simeq 15\%$. The results give evidence for a power law relationship $Nu_0 \propto Re^n$. The obtained exponent $n = 0.32 \pm 0.06$ is smaller than those reported for steady impinging jets ($0.5 < n < 0.8$) [8].

Kercher et al. [16] confirm a power law relationship between Nu_0 and Re for an impinging synthetic jet, albeit for a limited range of Re and for an unspecified range of stroke lengths. The results presented here show the explicit dependence of Nu_0 on both Re and L_0, for a fixed jet-to-surface spacing $H/D = 2$.

3.3 Vortex impingement at high stroke length

This section closely examines the fluid dynamics of the vortex impingement process and its influence on the local heat transfer rate. All results discussed below are for one selected synthetic jet setting of $L_0/D = 8.7$ and $Re = 1020$. Thus, the ratio of stroke length to jet-to-surface spacing $L_0/H = 8.7/2 = 4.35$ is greater than the critical value ($L_0/H = 4.35 > 2.5$).

3.3.1 Vortex dynamics

Figure 6 shows the phase-resolved evolution of the vortex characteristics during the process of formation, detachment, impingement, radial stretching and breakup into turbulence, spanning a phase interval of 480° or 4/3 cycles. The vortex strength and size are indicated by the thick lines representing the equiv-

alent circulation Γ_1 and radius r_1', respectively. The location of the vortex centre is indicated by the thin lines representing the vortex distance to the heat transfer surface $H - x_c$ and its radial position r_c. The horizontal axis indicates the phase with respect to the phase of maximum ejection θ_{max}. As such, $\theta - \theta_{max} = 0°$, 90°, 180° and 270° correspond respectively to peak ejection, end ejection, peak suction and end suction. The vertical dotted lines correspond to the phases listed in Table 1.

Table 1 lists the characteristics at eight distinct phases in the vortex impingement process, identified from Fig. 6 and listed below. Figure 7 shows the instantaneous vorticity field at each of these phases. The contour lines indicate the vorticity $\omega D(\theta)/U_0$, with a contour spacing increasing from 1/8 up to 4 in powers of 2. The path of the vortex centre $\{x_c, r_c\}$ in the left half plane (starting at $\theta_{(a)}$) is indicated by the thick solid line and crosshair marker.

(a) Leading up to the peak ejection, the developing vortex increases in strength and size (Fig. 7a).

(b) Around the peak ejection phase ($\theta = \theta_{max}$), the vortex detaches from the orifice and attains its maximum strength (Fig. 7b).

(c,d) Upon impingement (Fig. 7c and d), Fig. 6 shows that the vortex strength and size suddenly decrease to a minimum.

(e) Fed by the final part of ejection phase, the vortex recovers and attains its maximum strength after impingement (Fig. 7e). Afterwards, Fig. 6 shows that the vortex moves rapidly radially outward to $r_c/D \simeq 2.2$.

(f) The vortex continues to lose strength yet remains quasi stationary at $r_c/D \simeq 2.2$ until the end of the suction phase ($\theta = \theta_{max} + 270°$) (Fig. 7f). Only after the start of the next ejection phase does the vortex continue to move further outwards.

(g) Following the impingement of the new vortex, the old vortex moves upwards away from the surface (Fig. 7g). Note that angles $\theta_{(g)}$ and $\theta_{(e)}$ differ by 360°, thus show the same vorticity field but illustrate the distance traveled by the vortex during one cycle.

(h) Shortly after, the vortex completely loses coherence and dissipates into turbulence (Fig. 7h).

3.3.2 Effect on the local heat transfer

Figure 8 shows the effect of the vortex impingement on the radial profile of the time-averaged local heat transfer coefficient. The heat transfer coefficient has been determined using a uniform wall temperature surface and a thermopile heat flux sensor, which results in a superior spatial resolution compared to the heated foil. The top plot shows the local Nusselt number, normalized with its stagnation value. As an indication, the bottom plot shows the vortex path and eight circles corresponding to the vortex location at the phases in Table 1 and Fig. 7. The circle radius and line thickness indicate the equivalent vortex radius r_1' and strength, respectively.

Although Fig. 8 shows only time-averaged heat transfer data, some interesting insights can be obtained by comparing to the vortex impingement dynamics shown in Figs. 6 and 7.

The heat transfer coefficient peaks at the stagnation point and remains high up to $r/D \simeq 0.75$ (first vertical dotted line in Fig. 8) before dropping off sharply. The extent of the high heat transfer region may be explained based on the flow field results during vortex impingement (Fig. 7c-e). As Table 1 indicates, the vortex centre is at $r_c/D = 0.89$ upon impingement (Fig. 7c).

Furthermore, since the stroke length in this case is much greater than the jet-to-surface spacing ($L_0/H = 8.7/2 = 4.35$), the flow continues to impinge on the central region ($r/D < 0.75$) during the remainder of the ejection phase (Fig. 7d,e).

The heat transfer decreases monotonously with increasing radius. At $2.5 < r/D < 3$, a modest secondary peak can be identified, which also marks the radius of influence of the jet (second vertical dotted line in Fig. 8). Interestingly, $r_c/D = 2.2$ corresponds to the location where the vortex remains stationary up to the end of the suction phase (see Fig. 7d-f). As shown in Fig. 7g-h, the vortex moves away from the surface at $r_c/D = 3$ after the following vortex impingement, and subsequently dissipates into turbulence. As such, the extent of the coherent vortex corresponds to the radius of influence in terms of the heat transfer.

4 Conclusion

This paper presents phase-resolved flow field and time-averaged local heat transfer data for a round impinging synthetic jet, with a small jet-to-surface spacing $H/D = 2$.

The flow field characteristics have been investigated using particle image velocimetry (PIV), revealing the effect of the main synthetic jet parameters L_0/D and Re. For this fixed jet-to-surface spacing, two different flow regimes can be identified. For large stroke lengths at $L/D > 5$, a time-averaged recirculating vortex is established at $r/D \simeq 2$. Since the distance traveled by a propagating vortex scales with the stroke length [2], it is expected that

the ratio of stroke length to jet-to-surface spacing L_0/H determines the flow regime.

Heat transfer measurements have been performed using a heated foil surface and a thermal imaging camera. Based on the stagnation Nusselt number Nu_0, a critical stroke length $L_0/D = 5$ (or $L_0/H = 2.5$) has been identified. This is the same critical value that marks two flow regimes as observed from the PIV measurements.

There is evidence for a power law relationship between Nu_0 and Re with an exponent $n = 0.32 \pm 0.06$. The stagnation heat transfer is well described by a bilinear correlation (Eq. (3)).

Additional local heat transfer measurements have been performed using an isothermal copper plate and thermopile heat flux sensor, featuring a higher spatial resolution. Features in the local heat transfer profile can be explained by comparison to the impinging vortex dynamics.

For a selected case where the ratio of stroke length to jet-to-surface spacing is greater than the critical value ($L_0/H = 4.35 > 2.5$), the extent of the central region of high heat transfer ($r/D < 0.75$) corresponds roughly to the vortex impingement location. The region of influence for the heat transfer $r/D < 3$ seems to be determined by the distance traveled by the coherent vortex, before it dissipates into turbulence.

Further understanding of the heat transfer mechanisms could be obtained using time-resolved heat transfer measurements, which is the focus of ongoing research. However, the present paper already brings several new insights into the behaviour of the impinging vortex in a round synthetic jet, and its signif-

icance for the time-averaged heat transfer distribution.

Acknowledgements

Dr. Tim Persoons is a Postdoctoral Research Fellow of the Irish Research Council for Science, Engineering and Technology (IRCSET). The authors further acknowledge the financial support of Science Foundation Ireland (grant 07/RFP/ENM123). This work is performed in the framework of the Centre for Telecommunications Value-Chain Research (CTVR).

References

[1] R. Holman, Y. Utturkar, R. Mittal, B. Smith, L. Cattafesta, Formation criterion for synthetic jets, AIAA Journal 43 (10) (2005) 2110-2116.

[2] J.M. Shuster, D.R. Smith, Experimental study of the formation and scaling of a round synthetic jet, Physics of Fluids 19 (4) (2007) 045109.

[3] M.B. Gillespie, W.Z. Black, C. Rinehart, A. Glezer, Local convective heat transfer from a constant heat flux flat plate cooled by synthetic air jets, Journal of Heat Transfer 128 (10) (2006) 990–1000.

[4] B.L. Smith, A. Glezer, The formation and evolution of synthetic jets, Physics of Fluids 10 (9) (1998) 2281–2297.

[5] A. Pavlova, M. Amitay, Electronic cooling using synthetic jet impingement, ASME Journal of Heat Transfer 128 (9) (2006) 897-907.

[6] J.S. Campbell, W.Z. Black, A.Glezer, J.G. Hartley, Thermal management of a laptop computer with synthetic air microjets, Proc. IEEE In-

tersociety Conference on Thermal and Thermomechanical Phenomenon in Electronic Systems, pp.43-50, 1998.

[7] T.S. O'Donovan, D.B. Murray, Jet impingement heat transfer - Part I: Mean and root-mean-square heat transfer and velocity distributions, International Journal of Heat and Mass Transfer 50 (17-18) (2007) 3291-3301.

[8] T. Liu, J.P. Sullivan, Heat transfer and flow structures in an excited circular impinging jet, International Journal of Heat and Mass Transfer 39 (17) (1996) 3695-3706.

[9] A. McGuinn, T. Persoons, P. Valiorgue, T.S. O'Donovan, D.B. Murray, Heat transfer measurements of an impinging synthetic air jet with constant stroke length, Proc. European Thermal-Sciences Conference, Eurotherm, Eindhoven, The Netherlands, 18-22 May 2008.

[10] T. Persoons, T.S. O'Donovan, A pressure-based estimate of synthetic jet velocity, Physics of Fluids 19 (12) (2007) 128104.

[11] M. Raffel, C. Willert, J. Kompenhans, Particle image velocimetry, a practical guide, Springer-Verlag, 1998.

[12] T. Persoons, T.S. O'Donovan, D.B. Murray, Improving the measurement accuracy of PIV in a synthetic jet flow, Proc. Int. Symp. on Applications of Laser Techniques to Fluid Mechanics, Lisbon, Portugal, 2008.

[13] T. Persoons, T.S. O'Donovan, Multi double-frame particle image velocimetry, Measurement Science and Technology (in review).

[14] H. Vollmers, Detection of vortices and quantitative evaluation of their main parameters from experimental velocity data, Measurement Science and Technology 12 (2001) 1199-1207.

[15] P.G. Saffman, Vortex Dynamics, Cambridge University Press, 1992.

[16] D.S. Kercher, J.B. Lee, O.Brand, M.G. Allen, A. Glezer, Microjet cool-

ing devices for thermal management of electronics, IEEE Transaction on Components and Packaging Technologies 26 (2) (2003) 359-366.

Figure captions

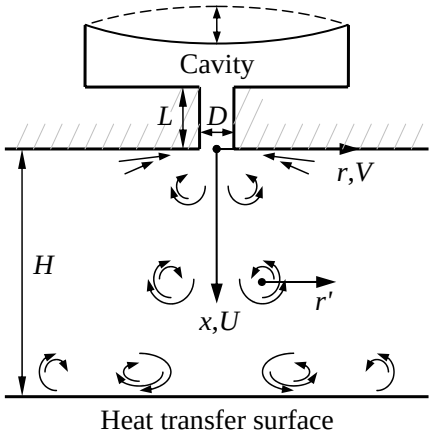

Fig. 1. Impinging synthetic jet nomenclature

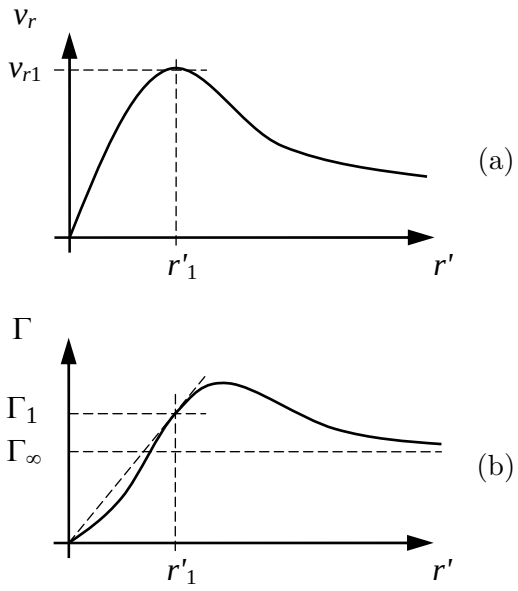

Fig. 2. Radial profile of (a) tangential velocity v_r and (b) circulation Γ for a viscous Lamb-Oseen vortex [15], in a frame of reference moving with the vortex centre

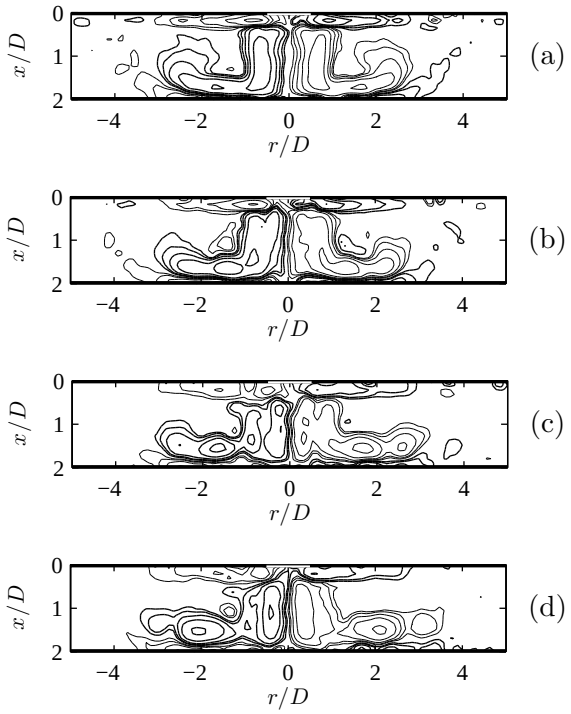

Fig. 3. Contours of time-averaged vorticity $\omega D/U_0$ for varying stroke length (a) $L_0/D = 2.48$, (b) $L_0/D = 3.78$, (c) $L_0/D = 5.04$, (d) $L_0/D = 8.70$ and constant Reynolds number $Re \simeq 1020$. Contour levels are increasing from 1/32 to 1 in powers of 2

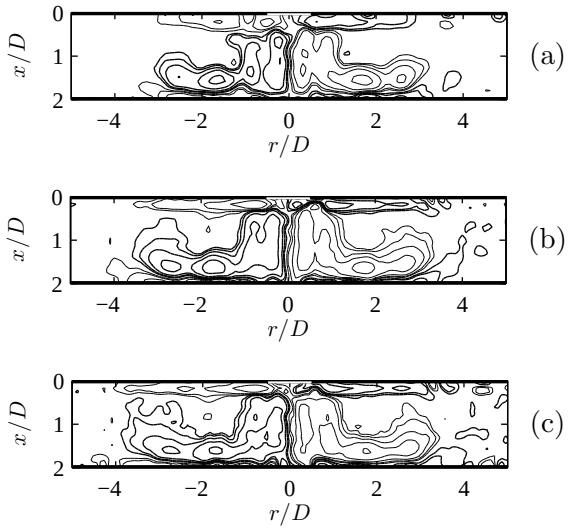

Fig. 4. Contours of time-averaged vorticity $\omega D/U_0$ for varying Reynolds number (a) $Re = 1010$, (b) $Re = 2010$, (c) $Re = 3000$ and constant stroke length $L_0/D \simeq 5.0$. Contour levels are increasing from 1/32 to 1 in powers of 2

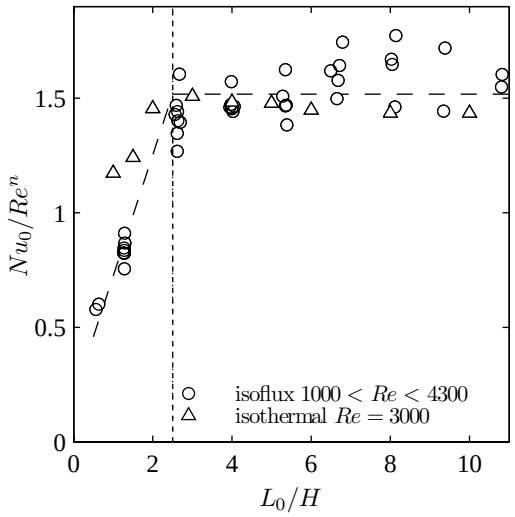

Fig. 5. Stagnation Nusselt number Nu_0 as a function of stroke length L_0/H for a single circular impinging synthetic jet at $H/D = 2$ ($1 < L_0/D < 22$, $1000 < Re < 4300$, $Pr = 0.71$), where $n = 0.32 \pm 0.06$ and $Nu_0/Re^n = 1.52 \pm 0.04$ ($L_0 > 2.5H$).

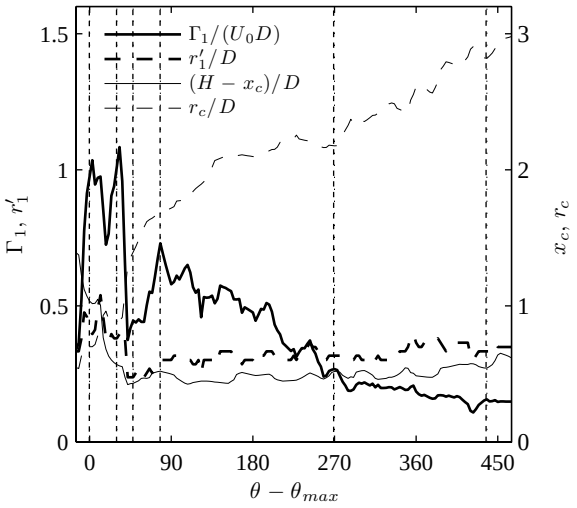

Fig. 6. Phase-resolved evolution of the vortex characteristics for $L_0/D = 8.7$ and $Re = 1020$

Table captions

Table 1

Vortex characteristics for $L_0/D = 8.7$ and $Re = 1020$ at eight characteristic phases

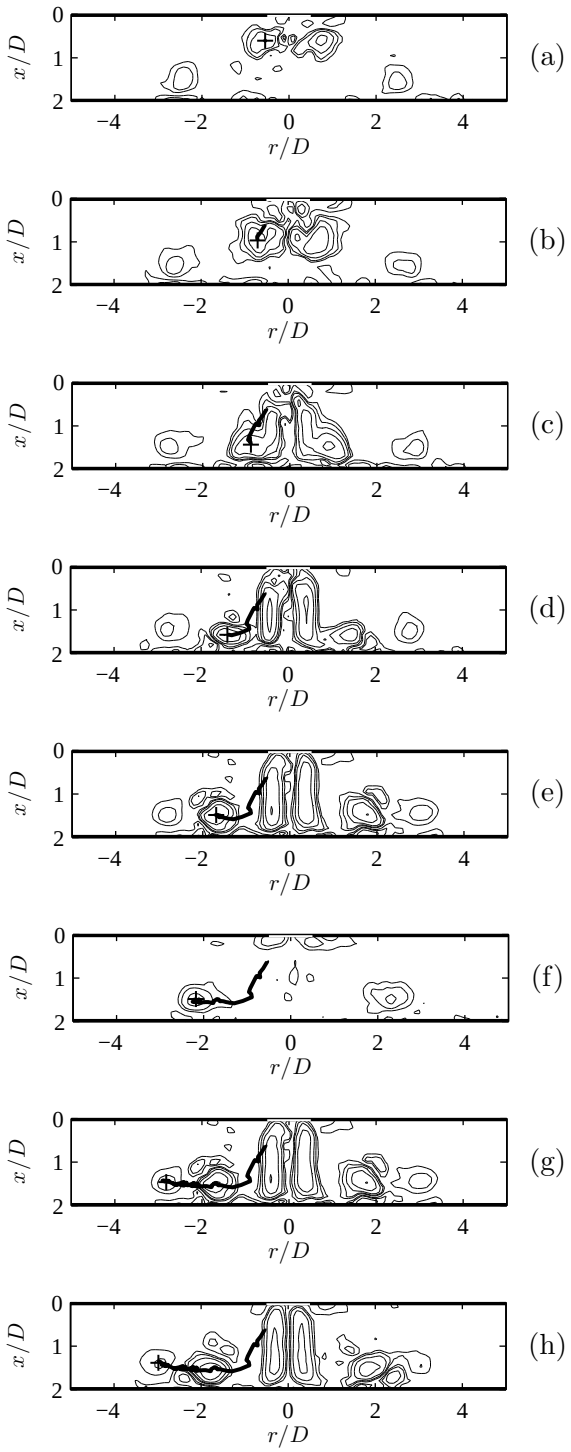

Fig. 7. Contours of phase-averaged vorticity $\omega(\theta)D/U_0$ for $L_0/D = 8.7$ and $Re = 1020$ at eight characteristic phases $\theta_{(a)}$ through $\theta_{(h)}$ (see Table 1). Contour levels are increasing from 1/8 to 4 in powers of 2

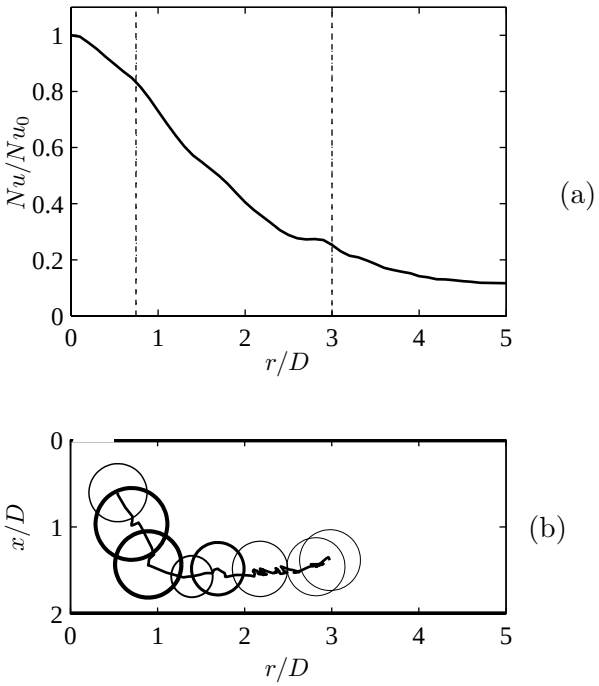

Fig. 8. Influence on (a) the local time-averaged heat transfer coefficient of (b) the impinging vortex (at phases corresponding to Table 1 and Fig. 7), for $L_0/D = 8.7$ and $Re = 1020$